Physica Scripta

INCLUSIVE PUBLISHING
TRUSTED SCIENCE

PAPER

Effect of divalent ion of strontium substitution on the structural, optical, magnetic and blood compatibility studies in cobalt ferrite

To cite this article: İ Ergin *et al* 2024 *Phys. Scr.* **99** 065908

View the article online for updates and enhancements.

You may also like

- Sr-doping effects on conductivity, charge transport, and ferroelectricity of $Ba_{0.7}La_{0.3}TiO_3$ epitaxial thin films
Qiang Li, , Dao Wang et al.
- Strengthening mechanism of Sr element on 6063 Al alloys
Zhan-Shou Yang, Yaping Dong, Wu Li et al.
- Electrochemical and Corrosion Response of Commercially Pure Aluminum Alloyed with Binary Additions of Strontium
N. L. Sukiman, H. Shi, R. K. Gupta et al.

This content was downloaded from IP address 193.140.54.155 on 15/05/2024 at 19:04

Physica Scripta

PAPER

Effect of divalent ion of strontium substitution on the structural, optical, magnetic and blood compatibility studies in cobalt ferrite

RECEIVED
3 January 2024

REVISED
26 February 2024

ACCEPTED FOR PUBLICATION
19 April 2024

PUBLISHED
30 April 2024

İ Ergin[1], S Özçelik[2], K İçin[3,4], B Yalcin[5], L Arda[6] and B Özçelik[1]

[1] Department of Physics, Faculty of Sciences and Letters, Çukurova University, 01330, Adana, Turkey
[2] Hakkari University, Faculty of Engineering, Department of Food Engineering, 30000, Hakkari, Turkey
[3] Department of Metallurgical and Materials Engineering, Faculty of Engineering, Karadeniz Technical University, Trabzon, Turkey
[4] Magnetic Materials Production and Design Applications and Research Center (MANYETAM), Karadeniz Technical University, Trabzon, Turkey
[5] Bahcesehir University, Vocational School of Health Services, Department of Medical Laboratory Techniques, 34353, Besiktas, Istanbul, Turkey
[6] Bahcesehir University, Faculty of Engineering and Natural Sciences, Department of Mechatronics Engineering, 34353, Besiktas, Istanbul, Turkey

E-mail: ozcelik@cu.edu.tr

Keywords: spinel ferrite, cobalt ferrite, nanoparticles, FT-IR, blood compatibility

Abstract

This study investigates the effects of Sr^{2+} substitution on the structural, morphological, and magnetic properties of magnetic cobalt ferrite ($CoFe_2O_4$). Through sol–gel auto-combustion synthesis, Sr^{2+} was substituted into Co-spinel ferrites ($Co_{1-x}Sr_xFe_2O_4$, where x = 0.0, 0.25, 0.5, 0.75, 1.0). SEM analysis revealed spherical grains with an average size of 54.4 nm. XRD analysis indicated systematic changes in crystallographic parameters and the formation of secondary phases with Sr-substitution. While the crystal size for $CoFe_2O_4$ was calculated as 262 nm, this value was determined as 18 nm for $Co_{0.25}Sr_{0.75}Fe_2O_4$. FT-IR results suggested increased force constants of octahedral and tetrahedral bonds with higher Sr content, with main vibration bands at 423.6 and 606 cm^{-1}. *M-H* curves exhibited *S*-shaped behavior, indicating drastic magnetic property changes with Sr^{2+} substitution. Coercivity field (*Hc*), saturation magnetization (M_S), and remanent magnetization (M_r) values ranged from 1447.8–545.4 Oe, 58.8-14 emu g^{-1}, and 36.8-7.6 emu g^{-1}, respectively. Blood compatibility experiments highlighted $Co_{0.75}Sr_{0.25}Fe_2O_4$ nanoparticles with significantly low hemolysis rates compared to other concentrations.

1. Introduction

The term 'spinel ferrite' is derived from the name of the mineral spinel, which is a naturally occurring material composed of metal oxides and other elements. The metal oxides are mixed in the form of a powder and then sintered in a furnace to form a ceramic material. Spinel ferrites are represented by a general formula AFe_2O_4, where A refers to the divalent metal cations [Ni^{2+}, Cu^{2+}, Mn^{2+}, Zn^{2+}, Co^{2+}, etc], can be depicted as a closely packed cubic structure of oxygen atoms with A^{2+} and Fe^{3+} at two different crystallographic regions [1, 2]. These regions are labelled as tetrahedral (A-site) and octahedral (B-site) oxygen coordination, respectively. The spinel structure is composed of two cation sites for cationic occupancy. There are 8 A-sites in which the metal cations are coordinated as tetrahedral with oxygen and 16 B-sites, which have octahedral coordination. When the A-sites are occupied by eight divalent A^{2+} cations and the B-sites are occupied by 16 trivalent ferric (Fe^{3+}) cations, the ferrite is named as a normal spinel. If the A-sites are completely occupied by one-half of Fe^{3+} cations and the B-sites are randomly occupied by A^{2+} and another half of Fe^{3+} cations, the structure is called an inverse spinel [3–5]. Spinel ferrites and their nanoparticles have attracted great interest from the research area due to their fascinating electrical and magnetic properties, such as high saturation magnetization, high Curie temperature, low eddy current losses, large magneto-crystalline anisotropy, low coercivity, high electric resistivity, high permeability, and mechanical hardness [6–11]. Due to their very interesting properties, most

© 2024 IOP Publishing Ltd

scientists have paid attention to spinel ferrites and their wide range of applicability for electronic applications such as magnetic media, gas sensors, microwave absorbers, high-density data storage, rechargeable lithium batteries, information storage systems, magnetic stack cores, and biological applications [12–22]. In addition, because of high coercivity, mechanical rigidity, conceivable magnetic saturation, magnetic anisotropy, excellent thermal and chemical stabilization characteristics, most of the spinel ferrite materials have become potential materials for several technological applications like spintronics, hyperthermia, molecular imaging applications, high frequency and power devices, supercapacitors, photocatalyst, and blood compatible nano-devices [23–29].

In recent years, advancements in ferrite nanomaterials have sparked significant interest across diverse fields, particularly in biomedical applications. Ferrites, owing to their unique magnetic and physicochemical properties, hold promise for various biomedical applications such as drug delivery, hyperthermia therapy, magnetic resonance imaging (MRI), and bioseparation processes [30, 31]. The nanoscale dimensions of ferrite particles enable enhanced surface area-to-volume ratios, which are advantageous for targeted drug delivery systems [32]. Additionally, the tunable magnetic properties of ferrites facilitate their use in magnetic hyperthermia therapy, where localized heating of tissues through the application of an external magnetic field can be utilized for cancer treatment [33]. Moreover, the magnetic properties of ferrites make them valuable contrast agents for MRI, providing enhanced imaging capabilities for disease diagnosis and monitoring [34]. Furthermore, ferrite nanoparticles have shown potential in bioseparation processes, aiding in the purification and isolation of biomolecules and cells [35]. The integration of ferrite nanomaterials into biomedical applications represents a burgeoning area of research with promising prospects for the development of innovative diagnostic and therapeutic strategies.

In the literature, there are a lot of approaches for nano-size spinel ferrite fabrication techniques, such as sol–gel combustion [36, 37], co-precipitation [38], microwave synthesis [39], auto-combustion [40], sol–gel [41] and micro-emulsion [42], laser ablation [43], and sono-chemical method [44].

Cobalt ferrite is a fascinating class of materials that belongs to the family of ferrites, which has an inverse-spinel crystal structure with Co^{2+} ions in the octahedral sites, whereas Fe^{3+} ions occupy octahedral and tetrahedral sites [36, 37]. There is great potential in the field of $CoFe_2O_4$ nanoferrites in various applications such as ferrofluid technology, cancer therapy, magnetic resonance imaging (MRI), and advanced microwave devices. These materials are highly regarded for their exceptional mechanical stiffness, persistent chemical stability, remarkable anisotropy ($K_\alpha = 3 \times 10^5$ J/m^3, significant and impressive saturation magnetization and coercivity values [45, 46]. The physical properties of these ferrites are highly dependent on a myriad of factors that include the intricacies of manufacturing techniques, chemical compositions, sintering temperatures, and the complex arrangement of cations within their crystal structure. In this regard, exploring the synthesis methods and characterization techniques and further understanding the structure–property relationship of cobalt spinel ferrite becomes crucial for optimizing its properties and expanding its applications. In many studies, doping and substitution ions were added instead of Co- or Fe- ions to improve the properties of Co-spinels. Mai M El-Masry *et al* doped Cu and Zn into Co-spinel structure to improve its thermal, electrical, mechanical and magnetic properties [47]. In another study, Cu was substituted for Co to examine the change in magnetic and elastic properties [48]. Due to the Cu^{+2} doping process, the optical energy gap of the nanoparticles exhibited a remarkable range from 1.77 eV to 2.20 eV. This variance in the energy gap suggests that these nanoparticles have considerable potential as candidates for water purification applications. In addition, it's worth noting that the saturation magnetization value experienced a significant increase, rising from an initial value of 79 emu g^{-1} to a higher and more favorable level of 106 emu g^{-1} [49]. This increase in saturation magnetization underscores the magnetic properties of the doped nanoparticles, further highlighting their suitability for a range of applications, including but not limited to water treatment and magnetic separation processes [49]. Therefore, in the present study, we aimed to modify the crystallite size of magnetic cobalt ferrite. Hence, nano-sized Sr^{2+}-ion-substituted Co-spinel ferrites, $Co_{1-x}Sr_xFe_2O_4$, where x = 0.0, 0.25, 0.5, 0.75, 1.0 have been fabricated via spontaneous sol–gel auto-combustion synthesis. We have, in detail, investigated the effect of Sr^{2+} inclusion for Co^{2+} with anticipation of a significant improvement in the structural, optical, magnetic and blood compatibility properties.

2. Experimental methods

$Co_{1-x}Sr_xFe_2O_4$ with x = 0.0, 0.25, 0.5, 0.75 and 1.0 nanoparticles were synthesized via sol–gel auto-combustion technique. In this method, iron(III) nitrate nonahydrate ($Fe(NO_3)_3.9H_2O$) was employed with a purity of 99.9%, along with cobalt(II) nitrate hexahydrate ($Co(NO_3)_2.6H_2O$) at max. 0.001% Ni. Additionally, strontium (II) nitrate ($Sr(NO_3)_2$) was used with a purity of 99.995%, and citric acid ($C_6H_8O_7$ _ 99% purity) was included as metal ion's complexant as well as the fuel of auto-combustion. 25% ammonia solution (NH_4OH) was used to adjust the pH value of the reaction media. Due to pH balance is important to provide a high surface area and

reduce the particle size the low pH value resulting from the presence of citric acid in the reaction medium was adjusted to pH = 7 using NH_4OH in order to form citric acid/M^{++} ion complexes ($[Sr_3(C_6H_5O_7)_2{\cdot}H_2O]$, $[Co_3(C_6H_5O_7)_2{\cdot}H_2O]$, etc) with high efficiency [50–52]. The all chemicals were purchased from Merck. The following chemical expression could be given for the synthesis of $Co_{1-x}Sr_xFe_2O_4$;

$$9(1-x)\,Co(NO_3)_2.6H_2O + 9xSr(NO_3)_2 + 18Fe(NO_3)_39H_2O + 26C_6H_8O_7 \rightarrow 9Co_{(1-x)}\,Sr_xFe_2O_4 + 156CO_2 + 45N_2 + 320H_2O$$

The total ratio of $Co(NO_3)_2.6H_2O$, $Sr(NO_3)_2$, $Fe(NO_3)_3.9H_2O$ and $C_6H_8O_7$ were selected as 1:2:2, respectively, and dissolved in 35 ml of distilled water with the aid of magnetic stirrer. Each sample solution was left in the atmospheric conditions for half an hour to obtain a homogeneous mixture. Then, NH_4OH was added dropwise into the acidic solution to achieve pH = 7, and after adding ammonia to the homogeneous solution, stirring proceeded for half an hour. Afterwards, the mixing process was stopped, and the heater was adjusted to 300 °C. Finally, the solution was turned into the gel phase through the boiling process, and then the residual gelous phase was dried, later, the powder materials in the vessel were ground in the agate mortar to eliminate the agglomeration.

The structural analysis, including lattice parameters and crystal size of the nanoparticle material, was carried out via the PANalytical X'pert Powder^3 diffractometer with a CuKα ($\lambda = 1.5418$ nm) radiation in the scanning range of $2\theta = 10°-80°$ with 0.013 °/sec increments, at room temperature. The surface morphologies and the phase composition of nanoparticles were investigated via the Zeiss EVO LS10 model scanning electron microscope (SEM) apparatus with secondary electron mode. BET (Brunauer, Emmett and Teller) analyses were applied to determine the surface areas. The degassing process was performed at 200 °C before each measurement of BET. The phase analysis was done with an energy-dispersive x-ray spectroscope (EDS) integrated into the SEM device. For the determination of the main spinel $Co_{1-x}Sr_xFe_2O_4$ structure and the presence of other covalent bonds, the Shimadzu IRSpirit model Fourier-transform infrared spectroscopy (FT-IR) was used in the range of 4000-400 cm^{-1}. With the aid of the Lake Shore 7304 model VSM system, the magnetic properties of nanoparticles were measured under ±1 Tesla magnetic field at room temperature.

The hemolytic potential of $Co_{1-x}Sr_xFe_2O_4$ nanoparticles against human erythrocyte cell membranes was investigated through hemolytic activity tests. Trisodium citrate (Na_3Ct-0.108 mM) was used to prevent the coagulation of blood samples drawn from healthy volunteers of 35–40 age. Blood:Na_3Ct ratio was adjusted as (9:1). Na_3Ct - blood mixtures were diluted with calcium and magnesium-free phosphate buffer solution (PBS) and then centrifuged at 4000 rpm for 5 min to separate the erythrocytes from blood plasma. PBS was prepared by the composition of NaCl (8 g/L), $Na_2HPO_4.2H_2O$ (1.78 g L^{-1}), $K^{-1}C^{-1}l^{-1}$ (0.2 g L^{-1}), and KH_2PO_4 (0.24 g L^{-1}), then autoclave-sterilised at 121 °C at 1 atm for 15 min. The erythrocyte deposit was then diluted up to 50 ml by adding PBS. Appropriate volumes of nanoparticle dispersions in PBS were mixed with 0.5 ml of RBC stock solution. The final concentrations of nanoparticles were adjusted as 0.5 m g /m l , 1.0 mg ml^{-1} and 3.0 mg ml^{-1}. Positive and negative control tests were conducted by using distilled water and PBS, respectively. In the positive control test, it was accepted that complete hemolysis of erythrocytes occurred with the hypertonic effect of distilled water (100%), while in the negative control test performed with PBS, it was accepted that the hemolysis was 0% in the erythrocytes treated in the isotonic medium. Erythrocytes were then incubated in the presence of nanoparticles at a physiological temperature (37 °C) for 3 h. Each test was repeated in duplicate, and an average of two separate experiments were reported. After incubation, erythrocyte-nanoparticle dispersions were centrifuged at 4000 rpm for 5 min. UV spectra for the supernatant of each sample were recorded to quantify the degree of hemolysis indicating cell lysis. The degree of hemolysis for each nanoparticle sample was calculated using the absorbance (ABS) value of the supernatant at 540 nm according to the expression given below [53].

$$\text{Degree of hemolysis} = \frac{ABS_{sample} - ABS_{negative\ test}}{ABS_{positive\ test} - ABS_{negative\ test}} \times 100 \quad (1)$$

3. Result and discussions

All structural, physical and biological findings of $Co_{1-x}Sr_xFe_2O_4$ with x = 0.0, 0.25, 0.5, 0.75 and 1.0 nanoparticles are in-depth, discussed and presented below.

3.1. Crystal structure properties

Figure1 presents the XRD powder patterns of $Co_{1-x}Sr_xFe_2O_4$ (x = 0.0, 0.25, 0.5, 0.75 and 1.0), nanoparticles taken between 10°– 80° diffraction angles. All ratios of Sr- substituted cobalt ferrite exhibited the characteristic spinel peaks belonging to the *Fd3m* space group cubic spinel structure, labelled as (111), (220), (311), (222),

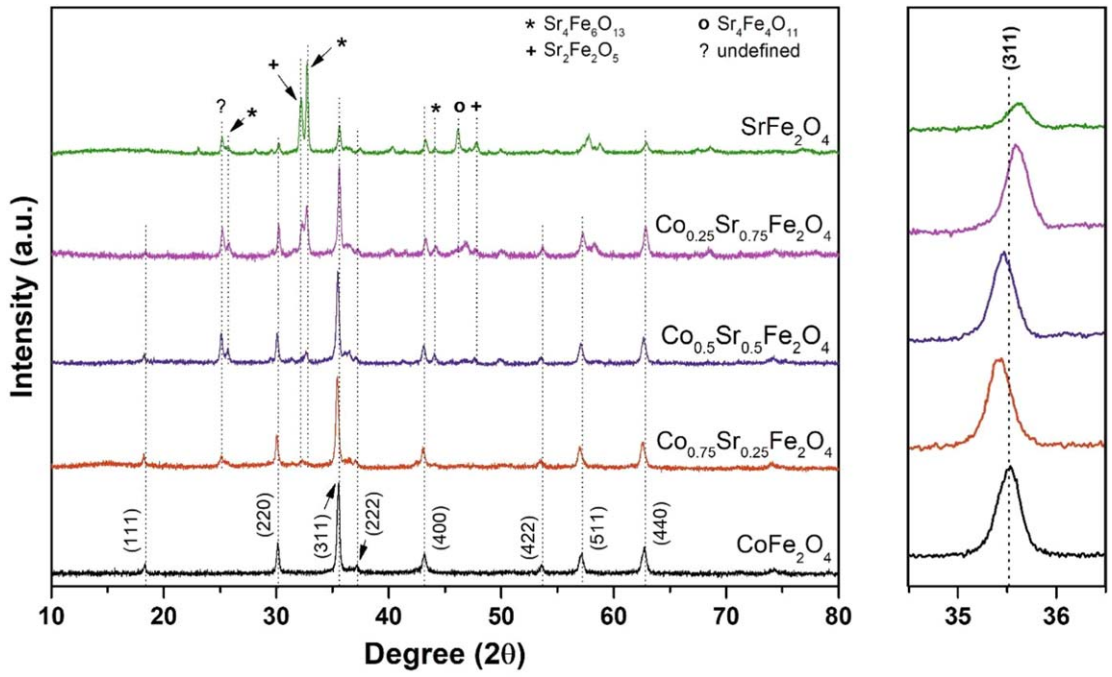


Figure 1. X-ray diffraction patterns of $Co_{1-x}Sr_xFe_2O_4$ ferrites and enlarged XRD patterns of (311) peak in the range of 34°–37°.

Table 1. Crystallographic and physical parameters of $Co_{1-x}Sr_xFe_2O_4$ ferrites.

Samples	*d-spacing (Å)*	*Strain (ε)*	*Crystal Size (D_{W-H}), nm*	*a, unit-cell (Å)*	*Cell Volume ($Å^3$)*	*Rietveld Analysis Results*		
						$CoFe_2O4$ (%)	*Other Phases (%)*	*χ2*
$CoFe_2O_4$	2.528	1.7×10^{-4}	262	8.384	589.30	96	4	1.12
$Co_{0.75}Sr_{0.25}$	2.535	5.7×10^{-4}	159	8.406	593.97	92	8	1.35
Co0.5Sr0.5	2.528	0.00252	7.4	8.383	589.11	86	14	1.22
Co0.25Sr0.75	2.522	0.00141	18	8.363	584.90	72	28	1.16
$SrFe_2O_4$	2.521	0.01828	42	8.359	584.06	—	100	1.21

(400), (422), (511), (440), corresponding to JCPDF card No.: 98-019-5863 catalog number. A few secondary peaks, namely $Sr_2Fe_2O_5$, $Sr_4Fe_6O_{13}$, and $Sr_4Fe_4O_{11,}$ were also observed and became more pronounced as each Sr contribution increased [54, 55].

The Rietveld analysis results in table 1 illustrate a clear correlation between the increasing presence of strontium and the higher proportions of strontium-containing phases within the samples. As the ratio of strontium increases from $CoFe_2O_4$ to $SrFe_2O4$, the percentage of strontium-containing phases gradually rises. Initially, in $Co_{0.75}Sr_{0.25}Fe_2O_4$, where strontium is present in a modest proportion, CoFe2O4 constitutes the primary phase at 92%, while other phases account for 8%. However, as the strontium content increases, as observed in $Co_{0.5}Sr_{0.5}Fe_2O_4$ and $Co_{0.25}Sr_{0.75}Fe_2O_4$, the percentage of other phases notably escalates to 14% and 28%, respectively. This underscores the significant impact of strontium increment on the overall composition and phase distribution in the analyzed samples. The reason why there are so many secondary phases is thought to be due to the ionic instability of the element Sr

The cubic unit cell parameter *a* and the crystal size of nanoparticles are calculated using equation (2) and equation (3), using XRD diffraction patterns results, respectively. Equation (3) is Williamson–Hall equation [56–58], which is used to calculate crystalline size and average lattice strain.

$$a_{exp} = d_{hkl}\,(h^2 + k^2 + l^2)^{1/2} \tag{2}$$

$$W\cos\theta_D = 4\varepsilon\sin\theta_D + \frac{K\lambda}{D} \tag{3}$$

where W is the full-width half maximum of the XRD peaks, λ is the wavelength of the used x-ray radiation ($\lambda_{Cu} = 1.54056$ Å), θ_D is the Bragg angle, and D is the average crystallize size. The relationship between W$\cos\theta_D$

and 4 $\sin\theta_D$ is described the strain ε of each XRD plot of the materials. The strain is inferred from the slope of the linear fitting data between $W\cos\theta_D$ and 4 $\sin\theta_D$, while the parameter D is determined from the Y-intercept ($K\lambda$/D). All calculated parameters of $Co_{1-x}Sr_xFe_2O_4$ nanoparticles are listed in table 1.

The table shows that the strongest maximum peak (311) is located at an angle $2\theta = 35.53°$ for pure cobalt ferrite and is increased $2\theta = 35.63°$ with doping Sr The Sr substitution reveals the strongest peak angle of cobalt spinel ferrite slightly shifted to the right of 0.10°. The cobalt ferrite sample's intensity decreases with strontium ions' presence.

The base compound, $CoFe_2O_4$, exhibits a standard d-spacing of 2.528 Å with minimal strain (1.7×10^{-4}). Its crystal size is relatively large at 262 nm, suggesting well-developed crystallites. The introduction of strontium in $Co_{0.75}Sr_{0.25}Fe_2O_4$ results in a slight increase in d-spacing (2.535 Å) and strain (5.7×10^{-4}), with a notable decrease in crystal size (159 nm), possibly due to strontium ions substitution to $CoFe_2O_4$ spinel structure. In $Co_{0.5}Sr_{0.5}Fe_2O_4$, with an equal ratio of cobalt and strontium substitution, the d-spacing returns to its base value (2.528 Å), while strain slightly increases (0.00252), indicating moderate lattice distortion. However, the crystal size significantly decreases to 7.44 nm, implying the presence of smaller crystallites. As the strontium ratio increases in $Co_{0.25}Sr_{0.75}Fe_2O_4$, the d-spacing decreases (2.522 Å), and strain decreases (0.00141), while crystal size increases of 18 nm. The absence of cobalt in $SrFe_2O_4$ alters the crystal structure, resulting in a higher strain of 0.01828 and a larger crystal size of 42 nm compared to cobalt-containing samples. Overall, these findings indicate that strontium incorporation affects the lattice parameters, strain, and crystal size of the ferrite compounds, influencing their magnetic properties and crystal structures. Higher strontium content tends to reduce d-spacing and strain while impacting crystal size and unit-cell parameters, highlighting the complex interplay between composition and structural properties in ferrite materials.

3.2. SEM analysis

The images obtained at high magnification (400kx) of $Co_{1-x}Sr_xFe_2O_4$ (x = 0.0, 0.25, 0.5, 0.75 and 1.0) nanoparticles using the back-scattering electrons mode of the SEM device were presented in figure 2. In the figure, the decreasing in the particle size can be seen with the increase of Sr doping until x = 0.5. The particle size images appearing in the figures were obtained by plotting the Gaussian function using the line intercept method and listed in table 2. It can be concluded that the average particle sizes of nanoparticles increase until the addition of x = 0.5 Sr, and with the subsequent doping, starts to decrease. The reason can be interpreted as the formation of new phases resulting from the different ionic structure of the Sr-element, which replaces the Co^{2+} ion, causing the formation of wide distribution particle size and a reduction in particle size.

The BET analysis results provided the specific surface area of different ferrite samples, with varying compositions involving strontium ion substitution. Interestingly, as the strontium ratio increases in the compositions from $CoFe_2O_4$ to $SrFe_2O_4$, there seems to be a fluctuation in the specific surface area. Notably, the $CoFe_2O_4$ sample exhibits a relatively high specific surface area of 130 m^2/g, followed by $Co_{0.75}Sr_{0.25}Fe_2O_4$ and $Co_{0.25}Sr_{0.75}Fe_2O_4$ with 126 m^2/g and 124 m^2/g, respectively. However, the sample with equal amounts of cobalt and strontium, $Co_{0.5}Sr_{0.5}Fe_2O_4$, shows a decrease in specific surface area to 103 m^2/g. The sample with solely strontium, $SrFe_2O_4$, displays the highest specific surface area of 141 m^2/g.

Figure 3 presents the EDS analysis of nanoparticles. According to these results, it is obtained that all peaks are relevant to the $Co_{1-x}Sr_xFe_2O_4$ material, confirming the presence of Co, Sr, Fe and O without impurities. According to the results of the analysis performed by using the entire area of the SEM image in the area spectrum distribution graphs in figure 3, although different phases are formed in the composition, the EDS analyzes show similarity with the composition formed within the error rates. When examining the EDS analyses of $CoFe_2O_4$ and $SrFe_2O_4$ compositions without substitution ions, it can be observed that the $CoFe_2O_4$ composition theoretically consists of 27.18 wt.% O, 46.80 wt.% Fe, and 26.87 wt.% Co. The EDS analysis measured the wt.% of O, Fe, and Co as 26.86%, 45.50%, and 26.00%, respectively. The $SrFe_2O_4$ compound should contain 24.31 wt.% O, 42.42 wt.% Fe, and 33.28 wt.% Sr according to theorical composition. EDS analysis determined the ratios of these ions to be 26.27 wt.% O, 42.22 wt.% Fe, and 31.51 wt.% Sr

3.3. FT-IR analysis

FT-IR spectroscopy is a good technique and the essential way to characterize the bonds in a molecule. As a result of the absorption of infrared radiation in the molecule, a series of vibrations in the molecular structure is created that form the basis of the FT-IR spectrum. In a definite range of infrared radiation, when the bonds of the molecule vibrate, the absorption process happens, and a peak arises, expressing the type, location and condition of the bonds. In the AB_2O_4 spinel structure, the typical characteristic tetrahedral A-O (ν_1) and the octahedral B-O (ν_2) bonds vibrate between 500–600 cm^{-1} and 400–500 cm^{-1} wavelengths, respectively. On the other hand, the standard metal-oxygen bond vibrates at a high frequency between 400–600 cm^{-1} wavelengths.

As a result of the FT-IR spectrum, two peaks between 400–600 cm^{-1} wavelengths may normally be observed pointing to the spinel structure. Figure 4 exhibits the infrared transmittance spectra of Sr-substituted Co-ferrite

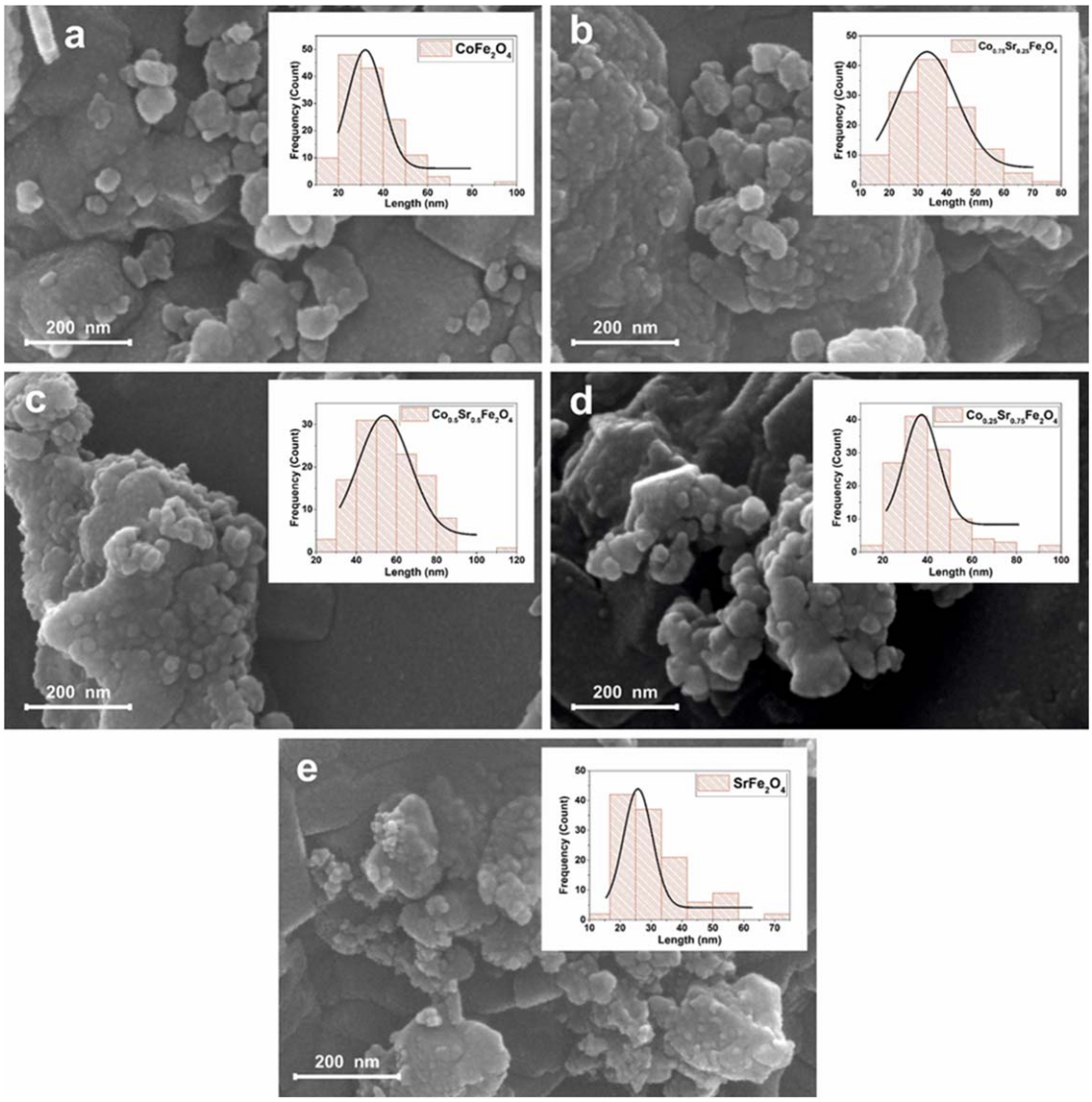


Figure 2. SEM micrographs and particle analysis of the $Co_{1-x}Sr_xFe_2O_4$ nanoparticles for (***a***) x = 0.00, (***b***) x = 0.25, (**c**) x = 0.50, (***d***) x = 0.75, and (***e***) x = 1.0.

Table 2. Some physical parameters deduced FT-IR spectra and average particle size analysis from SEM micrographs.

Samples	ν_O (cm^{-1})	ν_t (cm^{-1})	*Force Constant* (K_O) ($\times 10^2$ N/m)	*Force Constant* (K_t) ($\times 10^2$ N/m)	*Average Particle Size* (nm)
$CoFe_2O_4$	426.1	598.7	1.1	3.13	31.6
$Co_{0.75}Sr_{0.25}Fe_2O_4$	423.6	600.4	1.16	3.35	34.4
$Co_{0.5}Sr_{0.5}Fe_2O_4$	426.5	599.1	1.24	3.53	54.4
$Co_{0.25}Sr_{0.75}Fe_2O_4$	424.2	600.6	1.3	3.74	36.4
$SrFe_2O_4$	424.3	599.4	1.37	3.92	25.6

materials. In the figure, the vibrational frequencies of Sr-O or Co-O bonds (ν_1) and Fe-O bonds (ν_2) range lines up from 600.6 to 598.7 cm^{-1} and from 423.6 to 426.5 cm^{-1}, respectively [59, 60].

In addition, with the increase in Sr doping, the presence of C-O and O-H bonds was determined at approximately 880 and 1450 cm^{-1} wavelengths, respectively [61, 62]. These bonds in the matrix can be thought to be due to unburned citric acid residues since no heat treatment was applied to the materials after the sol–gel auto-combustion reaction.

According to the Waldron method [63] given in equation (4),

$$K_t = 7.62 \times M_1 \times v_1^2 \times \frac{10^{-7}N}{m} \quad (4)$$

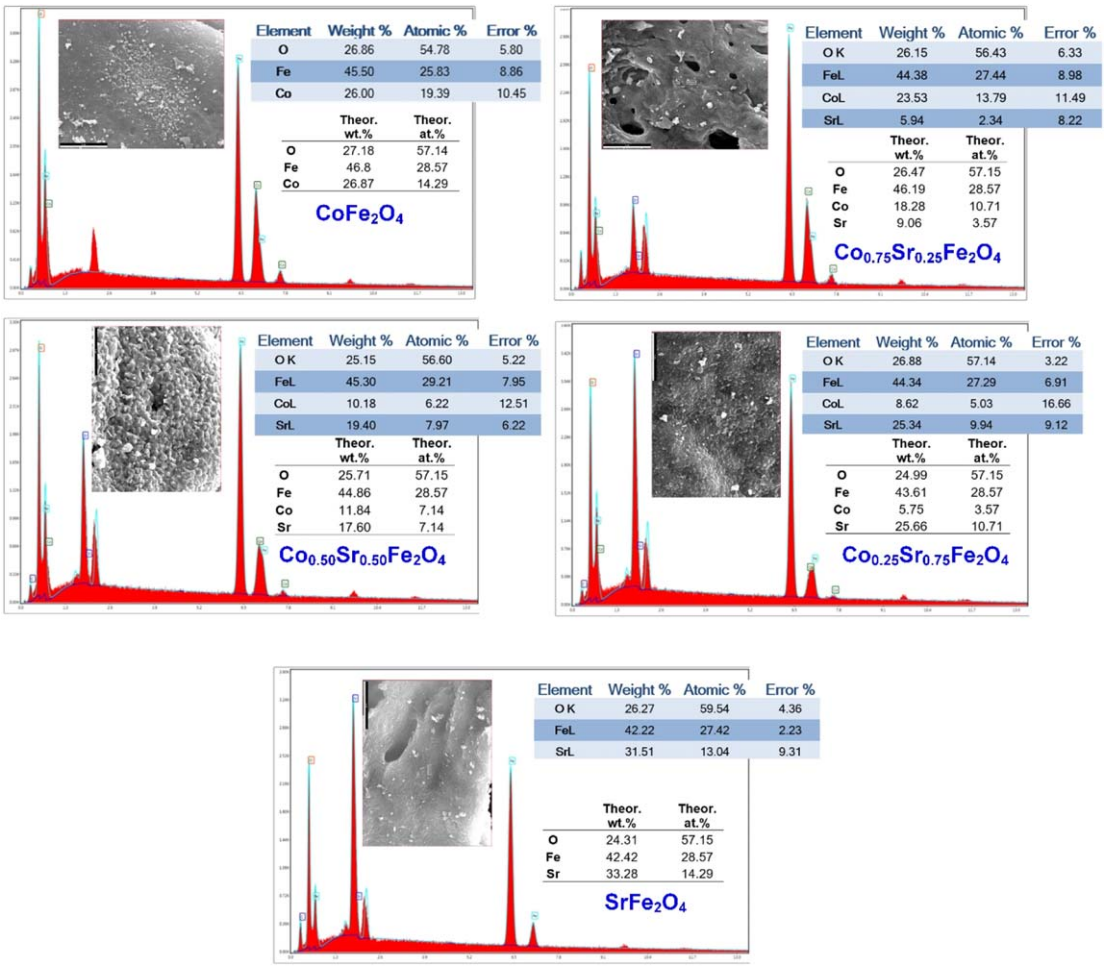


Figure 3. EDX spectra and elemental weight and numerical content of the $Co_{1-x}Sr_xFe_2O_4$ nanoparticles for (*a*) x = 0.00, (*b*) x = 0.25, (c) x = 0.50, (*d*) x = 0.75, and x = 1.0.

$$K_o = 5.31 \times M_2 \times v_2^2 \times 10^{-7} N/m$$

where M_1 and M_2 are the molecular weights of cations in A- and B-sites, respectively.

The estimated K_t and K_o values and frequency ranges are listed in table 2. As seen in the table, the force constants of the octahedral and tetrahedral bond increase with the increase of Sr content in the spinel ferrite system. It can be argued that substituting Sr^{2+} content in the tetrahedral site (A-site) successively transfers Co^{2+}, which is responsible for increasing the force constants. In other words, due to the substitution of Sr^{2+} ion, the charge imbalance in the matrix system happens, and hence, Fe^{3+} ions likely keep the oxygen ions, increasing the octahedral force constant [64].

3.4. Blood compatibility tests

The synthesis of ferrite-based nano-sized materials has become a remarkable research area due to the various potential applications of these materials. Nanoparticles with suitable mechanical and structural properties should be evaluated in terms of their biological properties, and it should be investigated whether they can be used in the medical field. Examining the hemolytic potential of a synthetic material is a practical and scientific way of determining the potential biocompatibility properties of the material towards living systems. In a related literature review, the *in vivo* biocompatibility of cobalt-doped Fe_2O_4 nanoparticles was investigated. In the study conducted on rabbits, $CoFe_2O_4$ synthesized by micro-emulsion method showed adverse effects on surgical sites of the kidney, liver, muscles as well as blood count [65]. Another study evaluating the biological properties of microwave-synthesized $CoFe_2O_4$ nanoparticles showed the non-toxic nature of these nanoparticles and recommended them to be used in biomedical applications [66]. Due to superparamagnetic properties, $CoFe_2O_4$ nanoparticles were offered as an alternative new material for magnetic hyperthermia applications and cancer therapy [67]. The impressive physicochemical properties of nano-sized $CoFe_2O_4$, such as stable structural and mechanical properties under physiological conditions and colloidal dispersion, make $CoFe_2O_4$ and its derivatives remarkable regarding biological applications. Inconsistency between hemoglobin and Fe-based

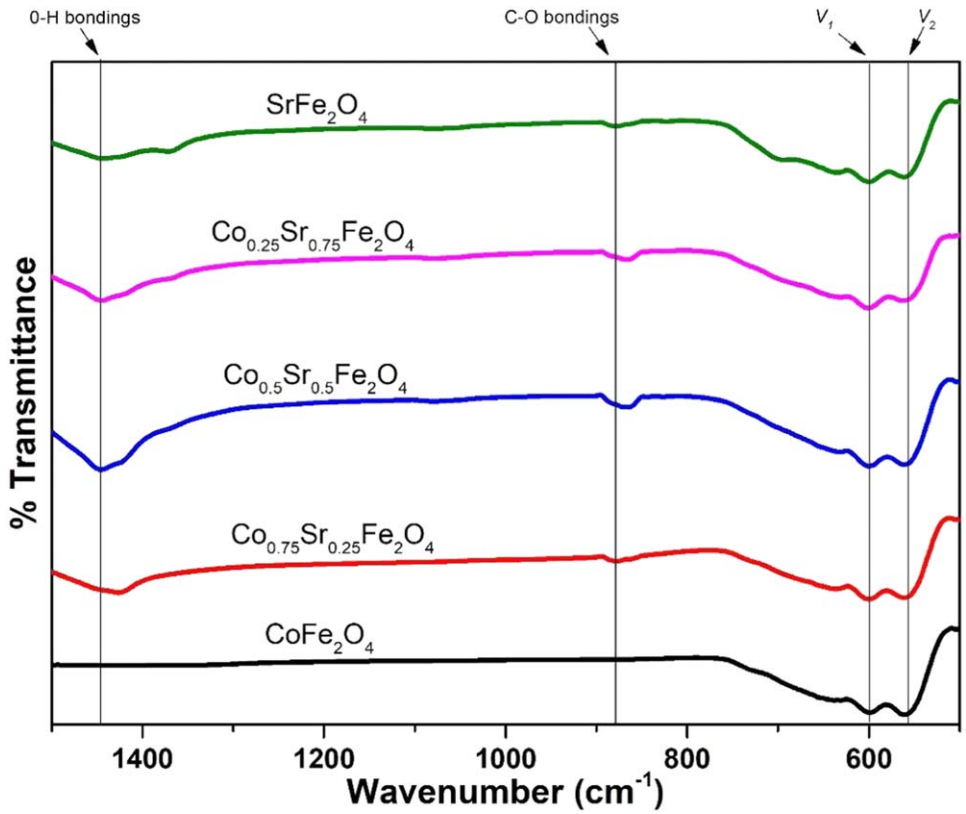


Figure 4. FT-IR spectra of $Co_{1-x}Sr_xFe_2O_4$ nanoparticles.

materials due to the presence of Fe in the structure could be prevented using ferrites, and better biological and biochemical properties such as enhanced tissue perfusion and blood compatibility could be generated [68].

It is known that nano-sized materials can change the erythrocyte morphology, disrupt the structural integrity of the erythrocyte cell membrane, and eventually cause hemolysis. This situation, which creates an inflammatory effect by suppressing the immune system and can cause autoimmune disorders and even cancer, is one of the most basic and observable negative interactions between nano-sized materials and blood. In this study, $Co_{1-x}Sr_xFe_2O_4$ nanoparticles were investigated in terms of their hemolytic potential as an indicator of blood compatibility. It has been observed that the peak intensities of the Soret band (416 nm) and Q bands (576 nm and 541 nm), which are the characteristic bands of the hemoglobin UV spectrum corresponding porphyrin $\pi-\pi^*$ transitions and ferrous heme (Fe^{2+}) in hemoglobin molecule respectively, increase with increasing nanoparticle concentration [69, 70] as seen in figure 5. In other words, as expected, hemolysis rates for all nanoparticles increased depending on the nanoparticle concentration as tabulated in table 3. Figure 6 shows the degree of hemolysis in erythrocyte suspensions treated with PBS alone (control) and $Co_{1-x}Sr_xFe_2O_4$ nanoparticles with three different concentrations, and those were 0.5 mg ml^{-1}, 1.0 mg ml^{-1}, and 3.0 mg ml^{-1}. All the hemolysis ratios at three different studied concentrations were less than 5%, which is the upper limit value for materials for biomedical purposes [ISO 10993-4]. However, a fluctuation in hemolysis percentages observed at equivalent concentrations of samples was also detected (table 3). This fluctuation in the results may depend on the resulting phases rather than the chemical composition. As stated in part 3.1, not all of the Sr ions added in place of Co settled in the $CoFe_2O_4$ crystal structure and new phases were formed. Thus, the fluctuation in hemolysis results can be attributed to the increasing ratio of different phases with increasing Sr content.

Although hemolysis rates below 5% were observed in all compositions, the highest percentage of hemolysis among the samples examined was observed in the $Co_{0.25}Sr_{0.75}Fe_2O_4$ at all three concentrations (0.5 mg ml^{-1}, 1.0 mg ml^{-1}, and 3.0 mg ml^{-1}). $Co_{0.25}Sr_{0.75}Fe_2O_4$ is also the composition in which other phases occur at the highest rate (28%), according to Rietveld Analysis results. Another effective parameter on erythrocyte hemolysis is the particle size of nano-sized materials. It has been stated that decreasing particle size may cause an increase in hemolysis rates [71–73]. Based on this, when the Rietveld analysis results and average particle sizes (tables 1 and 2) are evaluated together, it has been observed that the compositional properties and low percentages of other phases eliminate the hemolytic effect expected to arise from the slightly lower particle diameter (especially in the compositions of $CoFe_2O_4$ and $Co_{0.75}Sr_{0.25}Fe_2O_4$).

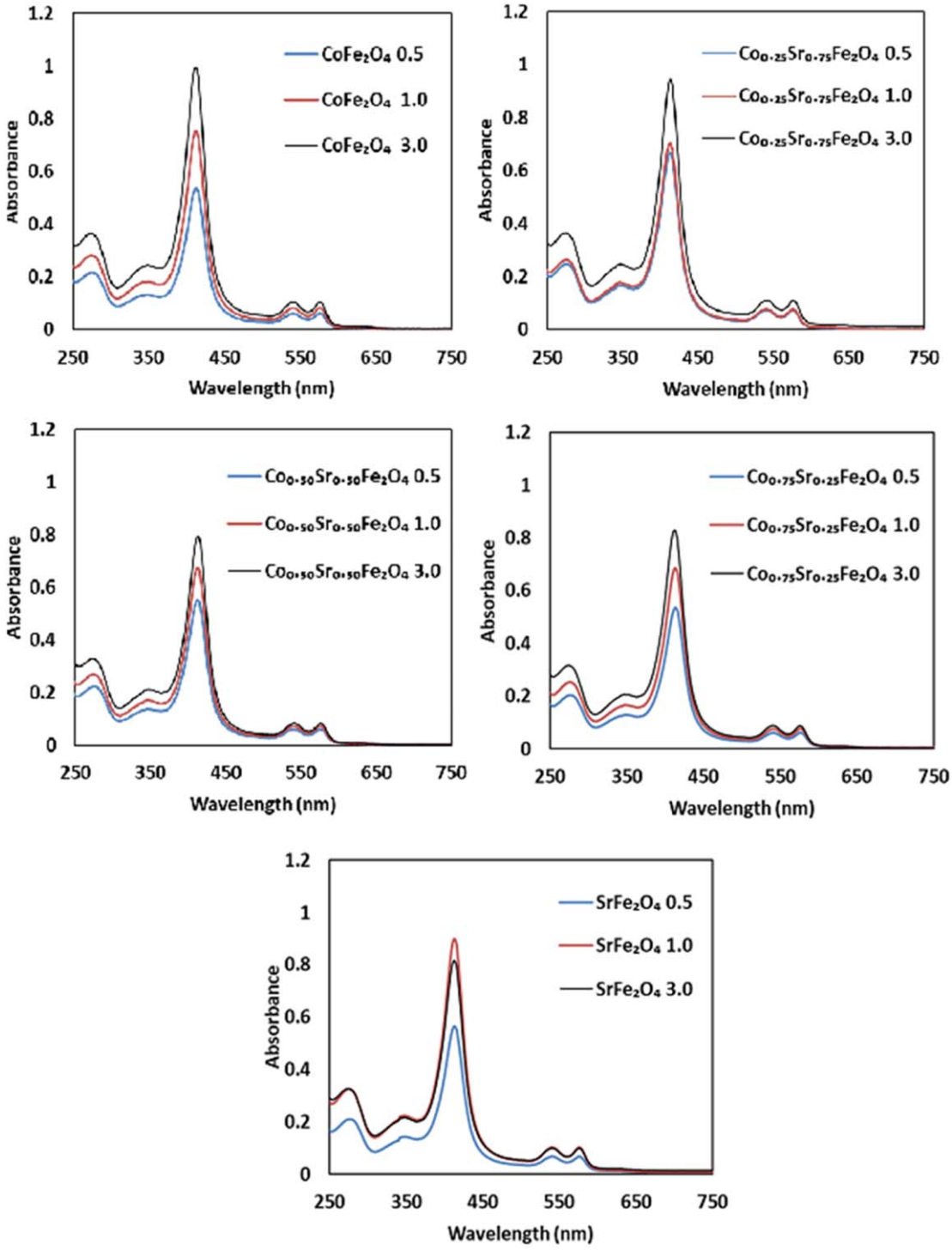


Figure 5. UV–vis spectra of erythrocyte suspensions treated with $Co_{1-x}Sr_xFe_2O_4$ nanoparticles with three different (0.5 mg ml-1, 1.0 mg ml^{-1} and 3.0 mg ml^{-1}) concentrations.

Other factors in the increase of hemolysis rates are the oxidative effect of reactive oxygen species produced by nanoparticles on the cell membrane and the physical interactions of nanoparticle-cell membranes. Erythrocyte cell wall composition has an affinity toward metal-oxide nanoparticles [74]. Therefore, nanoparticles can change the morphological structure of the cell membrane. Light microscope images of $Co_{0.25}Sr_{0.75}Fe_2O_4$ nanoparticles (3.0 mg ml^{-1}) presented explicit evidence of the effect of nanoparticles on the erythrocyte cell membrane. In figure 7(a), different types of deformations on erythrocyte membranes, such as echinocytes and acanthocytes with spicules on their surface, Heinz bodies, and eryptotic cells in the presence of 3.0 mg ml^{-1} of $Co_{0.25}Sr_{0.75}Fe_2O_4$ nanoparticles, were obvious. Variations in erythrocyte morphology mainly result from oxidative stress. Under the influence of oxidative stress, the characteristic biconcave shape of erythrocytes is distorted. Chemical interactions between heme unit and globin moieties of hemoglobin disrupt by ROS,

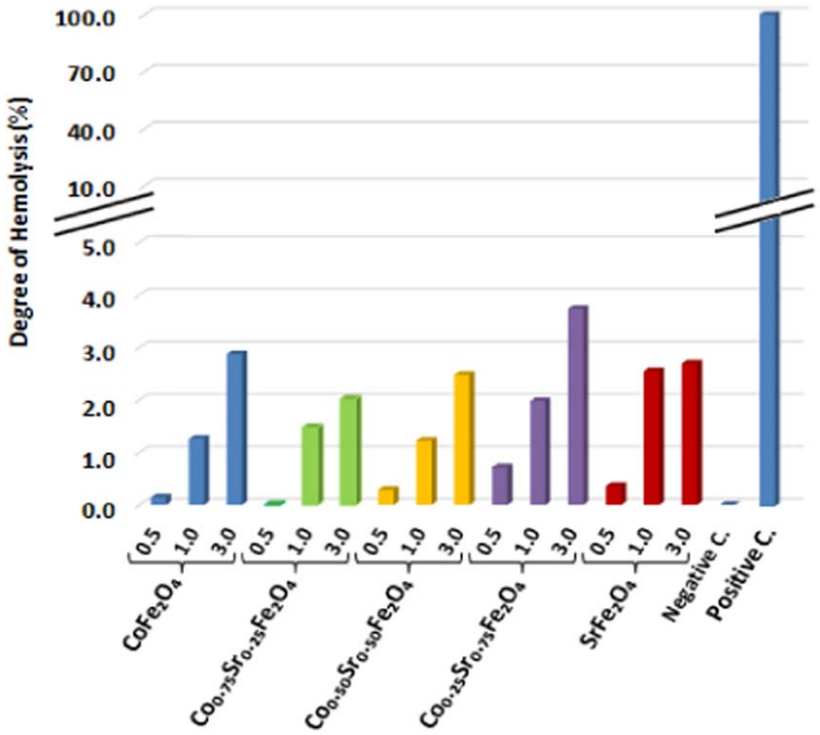


Figure 6. Hemolysis degree of $Co_{1-x}Sr_xFe_2O_4$ nanoparticles at three different concentrations. Hemolysis percentages in distilled water (positive control) and in PBS (negative control) are included.

Table 3. Degree of hemolysis in erythrocytes incubated in the presence of 3 different concentrations of $Co_{1-x}Sr_xFe_2O_4$ nanoparticles.

Sample	Concentration (mg ml^{-1})	Degree of Hemolysis (%)
$CoFe_2O_4$	0.5	0.14
	1.0	1.26
	3.0	2.87
$Co_{0.75}Sr_{0.25}Fe_2O_4$	0.5	0.00
	1.0	1.33
	3.0	2.01
$Co_{0.50}Sr_{0.50}Fe_2O_4$	0.5	0.29
	1.0	1.36
	3.0	2.48
$Co_{0.25}Sr_{0.75}Fe_2O_4$	0.5	0.72
	1.0	1.98
	3.0	3.74
$SrFe_2O_4$	0.5	0.36
	1.0	2.55
	3.0	2.69
Negative C.	—	0.0
Positive C.	—	100.0

resulting in the departure of globin units from hemoglobin. Aggregated globin fragments in the cell membrane form Heinz bodies, which cause complete lysis of erythrocytes with the effect of progressive oxidative stress [75].

It has been reported that magnetic Fe_3O_4 nanoparticles may lead to apoptosis of RBCs causing eryptosis and hemolysis in the early and later phases [76]. The acanthocyte development-triggering effects of titanium dioxide, silicon oxide, and iron oxide nanoparticles have also been emphasized by various literature studies [77–79]. Even the nanoparticles with the highest percentage of hemolysis at 3.0 mg ml^{-1} concentration among the samples examined had hemolysis value lower than the acceptable upper limit of 5%, changes in the morphological structure of some erythrocytes were observed under the light microscope (see figure 7). Various morphological defects were detected in RBCs treated especially with $Co_{0.25}Sr_{0.75}Fe_2O_4$ nanoparticles at 3.0 mg ml^{-1}, with a

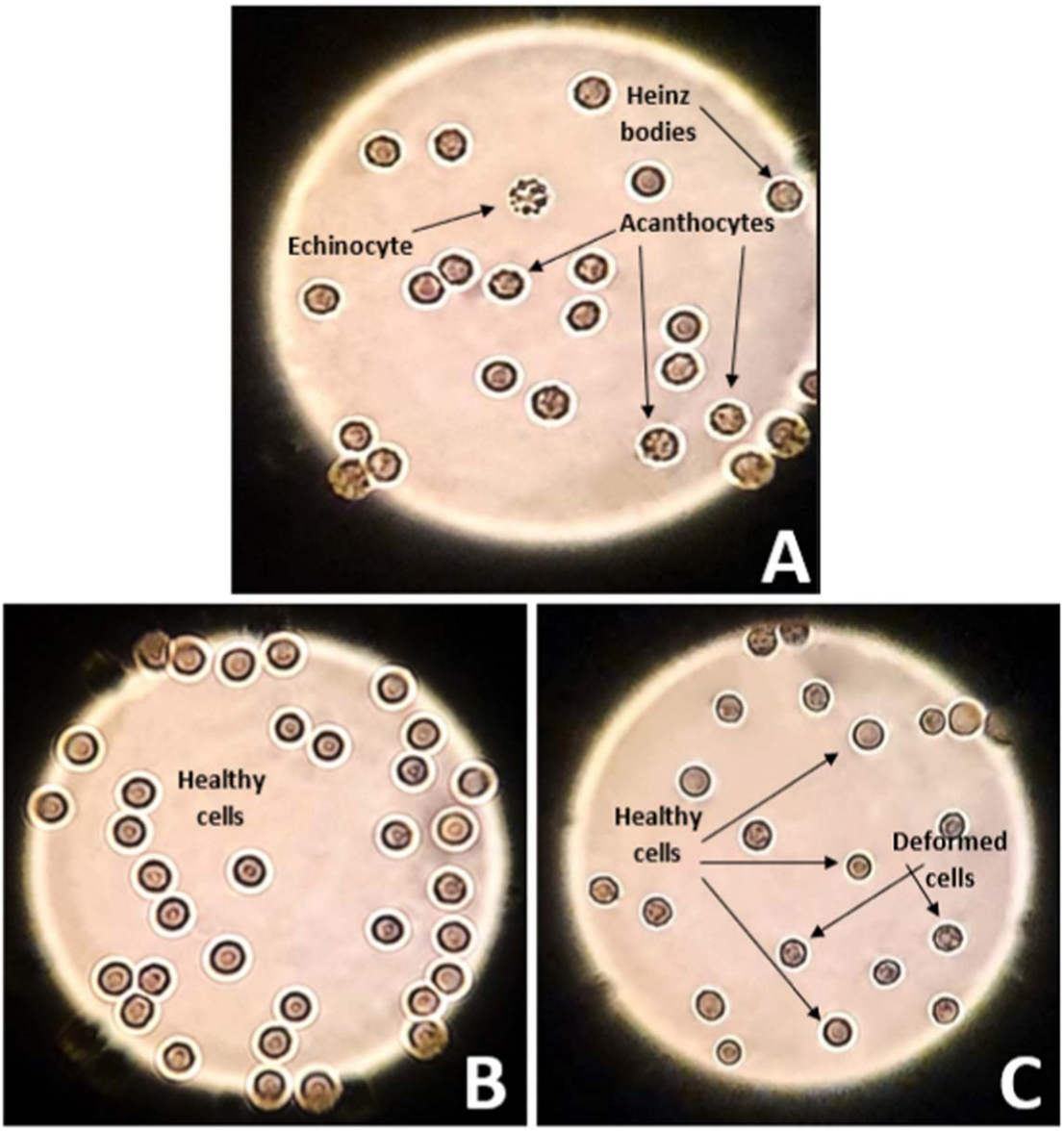


Figure 7. Light microscope image of (***a***) $Co_{0.25}Sr_{0.75}Fe_2O_4$ nanoparticles at 3.0 mg mL^{-1}, (***b***) $Co_{0.75}Sr_{0.25}Fe_2O_4$ nanoparticles at 0.5 mg mL^{-1} and (***c***) $Co_{0.75}Sr_{0.25}Fe_2O_4$ nanoparticles at 3.0 mg mL^{-1} (160x magnification).

prevalence of acanthocytes. This finding shows that although the upper limit of hemolysis accepted by the literature for materials to be used in the biological field is 5%, there are also some erythrocyte disorders that should be considered before complete erythrocyte lysis. Therefore, it is important to carry out studies at the cellular level in addition to instrumental analysis, especially in studies where the biocompatibility of nano-sized materials is examined. Figures 7(b) and (c) present light microscopy images of erythrocytes incubated in the presence of $Co_{0.75}Sr_{0.25}Fe_2O_4$ nanoparticles at concentrations of 0.5 and 3.0 mg.ml, respectively. Although no significant change was observed in erythrocyte morphology at 3.0mg.ml^{-1} concentration of $Co_{0.75}Sr_{0.25}Fe_2O_4$, which has a hemolysis degree of 2.1%, it was observed that erythrocytes had a wide range of distribution in diameter. In contrast, many healthy erythrocytes with a biconcave shape and equivalent diameters were observed at a concentration of $Co_{0.75}Sr_{0.25}Fe_2O_4$ 0.5 mg.ml^{-1}.

Among the samples examined in this study regarding blood compatibility, $Co_{0.75}Sr_{0.25}Fe_2O_4$ nanoparticles showed very low hemolysis rates at all three concentrations studied. According to the literature results, doping Sr^{2+} ions into TiO_2 nanoparticles significantly improves biological properties such as blood compatibility and cytocompatibility of endothelial cells [80]. It has also been stated that Sr can enhance the bioavailability of other biological-purpose materials, such as scaffolds having porous surfaces for cell attachment and growth [81, 82]. In this study, it was concluded that the biological properties were improved as a result of a synergistic effect between Sr and Co ions, which was evident at a critical concentration in $Co_{0.75}Sr_{0.25}Fe_2O_4$ nanoparticles where the Sr doping ratio was x = 0.25 [83].

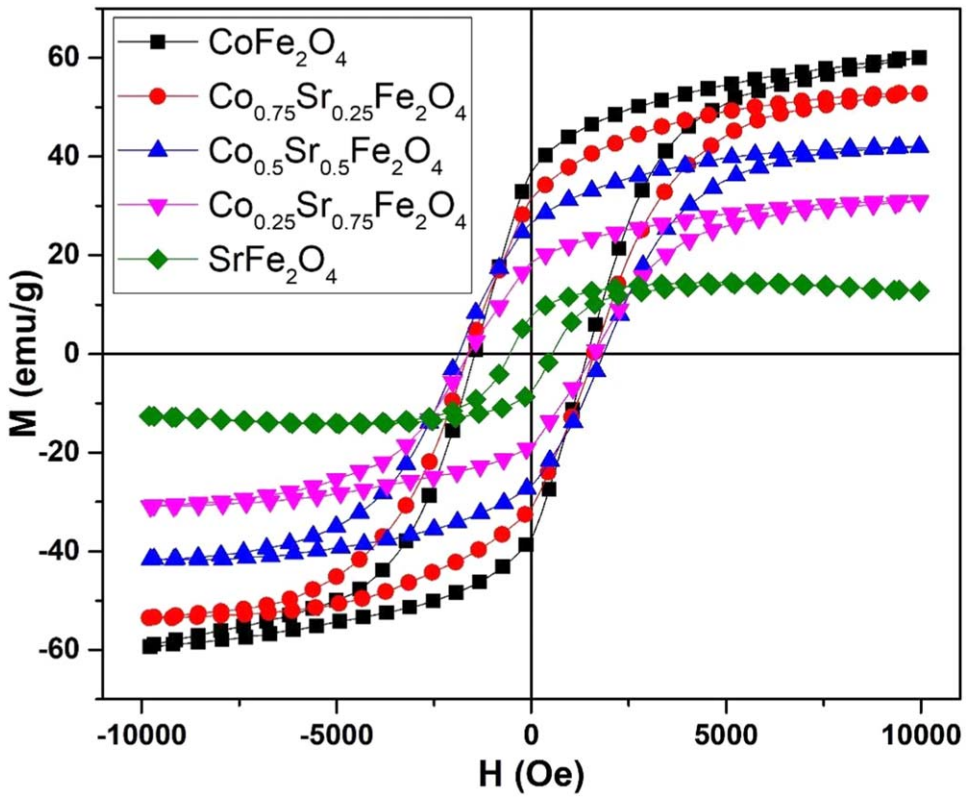


Figure 8. *M–H* curves measured at T = 300 K for $Co_{1-x}Sr_xFe_2O_4$ nanoparticles.

Table 4. The different magnetic parameters obtained from M-H hysteresis curves of $Co_{1-x}Sr_xFe_2O_4$ nanoparticles.

Samples	H_C *(Oe)*	M_R *(emu/g)*	M_S *(emu/g)*	β *constant* ($\times 10^8$)	K_α *anisotropy constant* ($\times 10^6$) *(erg/g)*
$CoFe_2O_4$	1447.8	36.8	58.8	−0.9855	1.122
$Co_{0.75}Sr_{0.25}Fe_2O_4$	1618	31.4	53.1	−0.89	0.915
$Co_{0.5}Sr_{0.5}Fe_2O_4$	1858.4	26.5	43	−0.7166	0.597
$Co_{0.25}Sr_{0.75}Fe_2O_4$	1608	18.6	31	−0.6815	0.495
$SrFe_2O_4$	546.4	7.6	14	+0.0208	0.039

3.5. Magnetic properties

The magnetic hysteresis loop results of $Co_{1-x}Sr_xFe_2O_4$ with x = 0.0, 0.25, 0.5, 0.75 and 1.0 nanoparticles, measured at room temperature and in the range of ±1 T external magnetic field were exhibited in figure 8. From the figure, it is seen that all samples have an S-shaped hysteresis curve. The magnetic quantities such as saturated (M_S) magnetization, remanent magnetization (M_R) and coercivity field values were tabulated in table 4. According to the table, M_R and M_S values systematically decreased with Sr-content increment. This decrease in saturation and remanent magnetizations can be attributed to the cation distribution of the sample. This decrease in remanent and saturation magnetizations can be identified by Sr-ions occupying the A-site (tetrahedral) or B-site (octahedral). The redistribution of cations in octahedral and tetrahedral sites is related to the presence of strains of force constants in metal bonds in octahedral or tetrahedral findings of FTIR spectra. It is also necessary to emphasize here that the reduction in the M_S can be attributed to the strain-induced magnetization due to the breaking of magnetic ion chains by substituting non-magnetic ions. This effect arises from the disruption of magnetic ion chains resulting from the substitution of non-magnetic ions of Sr^{2+}, in the crystal lattice. This interference leads to a systematic decrease in the overall magnetic response, as evidenced by the decreasing M_S values across the range of compositions studied.

In addition, the coercive field (H_C) of the Co/Sr- spinel ferrite enhanced from 1447,8 to 1858.4 Oe with the substitution of Sr-content up to x = 0.5, then it started to decrease with increasing Sr-content The initial increase in H_C can be attributed to a phenomenon known as domain wall pinning [84]. This phenomenon occurs at the surface of the nanoparticles. In simpler terms, it becomes progressively more challenging for the magnetic domains within the material to reorient themselves in response to an external magnetic field as Sr-content

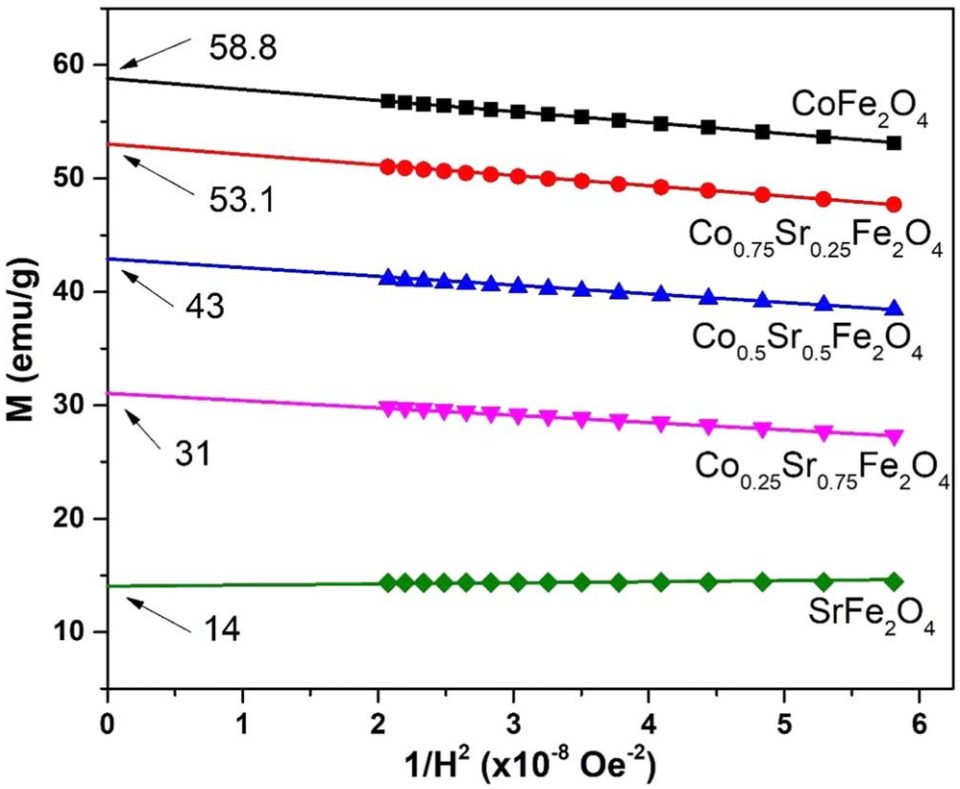


Figure 9. Plots of M versus $1/H^2$ obtained for $Co_{1-x}Sr_xFe_2O_4$ nanoparticles at T = 300 K.

increases. This is due to the presence of Sr-ions, which exert an influence on the magnetic moments within the samples, effectively 'pinning' or impeding the free movement of these magnetic domains. As a result, the hysteresis curve, the plot of magnetization against the applied magnetic field, becomes broader and more resistant to changes, as indicated by the rise in the coercive field. However, beyond a certain Sr-content threshold, this trend reverses, and the coercive field begins to decrease once more. This could be attributed to other competing factors coming into play, which may gradually weaken the domain wall pinning effect. These factors could include changes in the crystal structure, alterations in the cation distribution, or other intricate interactions within the material.

The field-dependent magnetisation in the region of saturation value is generally given by [85]

$$M = M_s\left[1 - \frac{\beta}{H^2}\right] \tag{5}$$

formula where M_S is the saturation magnetisation, β is a parameter relevant to the anisotropy of magneto-crystalline, and H is the external applied field. If the M versus $1/H^2$ graph is plotted as in figure 9, the saturation magnetisation (M_S) and β-value in the vicinity of room temperature are obtained by using fitting and the interception of the y-axis, respectively.

The magnetic anisotropy (K_a) constant can be conveniently deduced via the equation (6) [86];

$$K_a = M_s\sqrt{\frac{15\beta}{4}} \tag{6}$$

If the β values are deduced from figure 9, the magnetic anisotropy (K_α) values for all samples are obtained. The obtained data are tabulated in table 4.

4. Conclusion

In this study, the effect of Sr^{2+}-inclusions on the structural, physical, magnetical, morphological, Fourier Transform Infrared Radiation (FT-IR) and blood compatibility properties of $Co_xSr_{1-x}Fe_2O_4$ nanoparticles have been extensively presented. From the XRD patterns, the characteristic spinel peaks related to the *Fd3m* space group cubic spinel structure have been proved. It is also found that the diffraction angle, FWHM, d-spacing, crystallite sizes, *a*-parameter and cell volume values slightly changed by increasing Sr-content. Moreover, the main (311) peak has shifted towards higher angles with Sr-substitution. From SEM images, one can argue that

the average particle sizes of nanoparticles enhance up to x = 0.5Sr and then diminish with the subsequent doping. The magnetic results have shown that the saturation and remanent magnetization, the coercivity and the anisotropy constant have been prominently affected by Sr^{2+} substitution. From the blood compatibility results, it was concluded that the biological properties were improved due to a synergistic effect between Sr and Co ions, which was evident at a critical concentration x = 0.25. The Sr substituted $CoFe_2O_4$ nanoparticles were offered as an alternative new material for magnetic hyperthermia applications and cancer therapy [61, 75, 87].

The current study establishes Sr-substituted $CoFe_2O4$ nanoparticles as promising materials for magnetic hyperthermia applications and cancer therapy due to their tunable magnetic properties and improved blood compatibility. Future research could focus on optimizing the Sr content for enhanced magnetic and biological properties, exploring novel synthesis methods, and investigating the *in vivo* efficacy and safety of these nanoparticles for clinical applications. Additionally, further studies could explore the potential mechanisms underlying the observed improvements in blood compatibility and explore other biomedical applications beyond cancer therapy.

Acknowledgments

This study was carried out within the scope of Cukurova University Scientific Research Projects Unit FBA-2020-12956, FAY-2023-15808; the Scientific Research Project Coordination Center of Bahcesehir University (BAU) (Scientific Research Project Fund with the Project numbers BAP-2021.01.27).

Data availability statement

The data cannot be made publicly available upon publication because they contain commercially sensitive information. The data that support the findings of this study are available upon reasonable request from the authors.

Authors contribution

ibrahim Ergin: Material preparation, Data curation, Formal Analysis, ***Sezen Özçelik***: Contributor, Data curation, Formal Analysis. ***Kürşat için***: Material preparation, Data curation, Formal Analysis, ***Bestenur Yalçın***: Contributor, Data curation, Formal Analysis. ***Lütfi Arda***: Leader, Writing - Original Draft, Review & Editing. ***Bekir Özçelik***: Leader, Writing - Original Draft, Review & Editing.

Compliance with ethical standards

Approval Not applicable.

Conflict of interest

The author declares no competing interests.

ORCID iDs

S Özçelik https://orcid.org/0000-0003-2846-2226
K İçin https://orcid.org/0000-0002-5160-6753
B Yalcin https://orcid.org/0000-0002-7233-6561
L Arda https://orcid.org/0000-0003-0722-3891
B Özçelik https://orcid.org/0000-0002-8767-1426

References

[1] Mokhosi S R, Mdlalose W, Nhlapo A and Singh M 2022 Advances in the synthesis and application of magnetic ferrite nanoparticles for cancer therapy *Pharmaceutics* **14** 937
[2] Malik A Q, Singh H, Kumar A, Aepuru R, Kumar D, Mir T G, Ain Q, Bhat A A and Mubayi A 2023 An overview on magnetic separable spinel as a promising materials for photocatalysis and waste water treatment *ES Energy & Environment* **19** 744
[3] Tomar D and Jeevanandam P 2020 Synthesis of cobalt ferrite nanoparticles with different morphologies via thermal decomposition approach and studies on their magnetic properties *J. Alloys Compd.* **843** 155815

[4] Qin H, He Y, Xu P, Huang D, Wang Z, Wang H, Wang Z, Zhao Y, Tian Q and Wang C 2021 Spinel ferrites (MFe_2O_4): synthesis, improvement and catalytic application in environment and energy field *Adv. Colloid Interface Sci.* **294** 102486
[5] Narang S B and Pubby K 2021 Nickel spinel ferrites: a review *J. Magn. Magn. Mater.* **519** 167163
[6] Liu Q, Lv L, Zhou J-P, Chen X-M, Bian X-B and Liu P 2012 Influence of nickel-zinc ratio on microstructure, magnetic and dielectric properties of $Ni_{(1-x)}Zn_xFe_2O_4$ ferrites *J. Ceram Process Res.* **13** 110–6
[7] Mukherjee S, Pradip S, Mishra A K and Das D 2014 Zn substituted $NiFe_2O_4$ with very high saturation magnetization and negligible dielectric loss synthesized via a soft chemical route *Appl. Phys.* A **116** 389–93
[8] Ghasemi A and Mousavinia M 2014 Structural and magnetic evaluation of substituted $NiZnFe_2O_4$ particles synthesized by conventional sol–gel method *Ceram. Int.* **40** 2825–34
[9] Heiba Z K, Mohamed M B, Hamdeh H H and Ahmed M A 2015 Structural analysis and cations distribution of nanocrystalline $Ni_{1-x}Zn_xFe_{1.7}Ga_{0.3}O_4$ *J. Alloys Compd.* **618** 755–60
[10] Thanigai Arul K, Manikandan E, Ladchumananandasivam R and Maaza M 2016 Novel polyvinyl alcohol polymer based nanostructure with ferrites co-doped with nickel and cobalt ions for magneto-sensor application *Polym. Int.* **65** 1482–5
[11] Wu X, Chen W, Wu W, Li H and Lin C 2017 Structural and magnetic properties evolution of Li-substituted $Co_{0.5}Ni_{0.5}Fe_2O_4$ ferrite *J. Electron. Mater.* **46** 199–207
[12] Lee S W, Bae S, Takemura Y, Yamashita E, Kunisaki J, Zurn S and Kim C S 2006 Magnetic properties, self-temperature rising characteristics, and biocompatibility of $NiFe_2O_4$ nanoparticles for hyperthermia applications *IEEE Trans. Magn.* **42** 2833–5
[13] Tyagi S, Baskey H B, Agarwala R C, Agarwala V and Shami T C 2011 Development of hard/soft ferrite nanocomposite for enhanced microwave absorption *Ceram. Int.* **37** 2631–41
[14] Lin K S, Adhikari A K, Wang C Y, Hsu P J and Chan H Y 2013 Synthesis and characterization of nickel and zinc ferrite nanocatalysts for decomposition of CO_2 greenhouse effect gas *J. Nanosci. Nanotechnol.* **13** 2538–48
[15] Singh J, Roychoudhury A, Srivastava M, Chaudhary V, Prasanna R, Lee D W, Lee S H and Malhotra B D 2013 highly efficient bienzyme functionalized biocompatible nanostructured nickel ferrite–chitosan nanocomposite platform for biomedical application *J. Phys. Chem.* **117** 8491–502
[16] Leal E, Dantas J, Santos P T A, Bicalho S M C M, Kiminami R H G A, da Silva M R and Costa A C F M 2018 Effect of the surface treatment on the structural, morphological, magnetic and biological properties of MFe2O4 iron spinels (M = Cu, Ni, Co, Mn and Fe) *Appl. Surf. Sci.* **455** 635–45
[17] Wu K, Li J and Zhang C 2019 Zinc ferrite based gas sensors: A review *Ceram. Int.* **45** 11143–57
[18] Elayakumar K, Manikandan A, Dinesh A, Thanrasu K, Kanmani Raja K, Thilak Kumar R, Slimani Y, Jaganathan S K and Baykal A 2019 Enhanced magnetic property and antibacterial biomedical activity of Ce3+ doped CuFe2O4 spinel nanoparticles synthesized by sol-gel method *J. Magn. Magn. Mater.* **478** 140–7
[19] Acharya R, Pati S and Parida K 2022 A review on visible light driven spinel ferrite-g-C3N4 photocatalytic systems with enhanced solar light utilization *J. Mol. Liq.* **357** 119105
[20] Manohar A, Vijayakanth V, Vattikuti S V P and Kim K H 2022 A mini-review on AFe2O4 (A = Zn, Mg, Mn, Co, Cu, and Ni) nanoparticles: Photocatalytic, magnetic hyperthermia and cytotoxicity study *Mater. Chem. Phys.* **286** 126117
[21] Jose V, Jose V, Freeda Christy C E and Nesaraj A S 2022 Spinel-based electrode materials for application in electrochemical supercapacitors—present status and future prospects *Inorganic and Nano-Metal Chemistry* **52** 1449–62
[22] Li Y, Dang J, Ma Y and Ma H 2023 Hematite: a good catalyst for the thermal decomposition of energetic materials and the application in nano-thermite *Molecules* **28** 5
[23] Carey M J, Maat S, Rice P, Farrow R F C, Marks R F, Kellock A, Nguyen P and Gurney B A 2002 Spin valves using insulating cobalt ferrite exchange-spring pinning layers *Appl. Phys. Lett.* **81** 1044–6
[24] Lee J-H *et al* 2007 Artificially engineered magnetic nanoparticles for ultra-sensitive molecular imaging *Nat. Med.* **13** 95–9
[25] Torres T E, Roca A G, Morales M P, Ibarra A, Marquina C, Ibarra M R and Goya G F 2010 Magnetic properties and energy absorption of $CoFe_2O_4$ nanoparticles for magnetic hyperthermia *J. Phys. Conf. Ser.* **200** 072101
[26] Kalam A, Al-Sehemi A G, Assiri M, Du G, Ahmad T, Ahmad I and Pannipara M 2018 Modified solvothermal synthesis of cobalt ferrite ($CoFe_2O_4$) magnetic nanoparticles photocatalysts for degradation of methylene blue with H_2O_2/visible light *Results in Physics* **8** 1046–53
[27] Thomas B and Alexander L K 2018 Enhanced synergetic effect of Cr(VI) ion removal and anionic dye degradation with superparamagnetic cobalt ferrite meso–macroporous nanospheres *Appl. Nanosci.* **8** 125–35
[28] Liu J, Zhang L, Zang D and Wu H 2021 A competitive reaction strategy toward binary metal sulfides for tailoring electromagnetic wave absorption *Adv. Funct. Mater.* **31** 2105018
[29] Yalcin B, Ozcelik S, Icin K, Senturk K, Ozcelik B and Arda L 2021 Structural, optical, magnetic, photocatalytic activity and related biological effects of $CoFe_2O_4$ ferrite nanoparticles *J. Mater. Sci., Mater. Electron.* **32** 13068–80
[30] Phalake S S, Somvanshi S B, Tofail S A M, Thorat N D and Khot V M 2023 Functionalized manganese iron oxide nanoparticles: a dual potential magneto-chemotherapeutic cargo in a 3D breast cancer model *Nanoscale* **15** 15686–99
[31] Somvanshi S B, Patade S R, Andhare D D, Jadhav S A, Khedkar M V, Kharat P B, Khirade P P and Jadhav K M 2020 Hyperthermic evaluation of oleic acid coated nano-spinel magnesium ferrite: Enhancement via hydrophobic-to-hydrophilic surface transformation *J. Alloys Compd.* **835** 155422
[32] Kalaiselvan C R, Laha S S, Somvanshi S B, Tabish T A, Thorat N D and Sahu N K 2022 Manganese ferrite ($MnFe_2O_4$) nanostructures for cancer theranostics *Coord. Chem. Rev.* **473** 214809
[33] Sulttan S and Rohani S 2023 Modeling and simulation of smart magnetic self-assembled nanomicelle trajectories in an internal thoracic artery flow for breast cancer therapy *Drug Deliv. Transl. Res.* **13** 675–88
[34] Saeidi H, Mozaffari M, Ilbey S, Dutz S, Zahn D, Azimi G and Bock M 2023 Effect of europium substitution on the structural, magnetic and relaxivity properties of Mn-Zn ferrite nanoparticles: a dual-mode MRI contrast-agent candidate *Nanomaterials* **13** 331
[35] Toudeshkchouei M G and Abdoos H 2024 Magnetic nanoparticles fabricated/integrated with microfluidics for biological applications: A review *Biomed. Microdevices* **26** 13
[36] Kirankumar V S and Sumathi S 2019 Copper and cerium co-doped cobalt ferrite nanoparticles: structural, morphological, optical, magnetic, and photocatalytic properties *Environmental Science and Pollution Research* **26** 19189–206
[37] Ergin İ, İçin K, Güngüneş H and Özçelik B 2023 Detailed studies on structural, morphological, optical, magnetic and mossbauer properties of Cu-substituted cobalt ferrite nanoparticles *Phys. Scr.* **98** 035807
[38] Thakur P, Thakur P, Kishore K, Singh M, Sharma S, Sharma P, Sharma P and Lal M 2023 Structural, morphological, and magnetic properties of $CoFe_2O_4$ nano-ferrites synthesized via Co-precipitation route *Mater. Today Proc.* (https://doi.org/10.1016/j.matpr.2022.12.233)

[39] Ayyıldız M F, Karaman D N, Kartoğlu B, Şaylan M, Chormey D S and Bakırdere S 2023 A simple microwave-assisted synthesis of cobalt ferrite nanoparticles and its application for the determination of lead ions in rooibos (Aspalathus linearis) tea *Food Chem.* **429** 136862
[40] Khan N, Irshad I, Almutairi B S, Dahshan A, Husssain A, Tahir M B, Ahmed B and Sagir M 2024 Sol-gel auto-combustion synthesis and characterization of Nd3+ doped Cu0.5Co0.5Fe2-xNdxO4 (x = 0.0, 0.1, 0.2, 0.3, 0.4, & 0.5) spinel ferrites *Ceram. Int.* **50** 8594-8601
[41] Islam S, Lutfor Rahman M, Rassel Moni M, Biswas B, Farid Ahmed M and Sharmin N 2023 Impacts of annealing temperature on microstructure, optical and electromagnetic properties of zinc ferrites nanoparticles synthesized by polymer assisted sol-gel method *Arabian J. Chem.* **16** 105186
[42] Gilani Z A, Samiullah, Asghar H M N H K, Khalid M, Suleman M, Shar M A, Ali S M, Iqbal F and Alhazaa A 2023 Structural, dielectric and electric modulus analysis of praseodymium-substituted SrPrxFe12-X O19 nanoparticles synthesized via micro-emulsion *Appl. Phys.* **129** 145
[43] Özçelik S, Yalçın B, Arda L, Santos H, Sáez-Puche R, Angurel L A, Fuente G F and Özçelik B 2021 Structure, magnetic, photocatalytic and blood compatibility studies of nickel nanoferrites prepared by laser ablation technique in distilled water *J. Alloys Compd.* **854** 157279
[44] Akhtar S, Slimani Y, Almessiere M A, Baykal A, Polat E G and Caliskan S 2023 Influence of Tm and Tb co-substitution on structural and magnetic features of CoFe2O4 nanospinel ferrites *Nano-Structures & Nano-Objects* **33** 100944
[45] Sanpo N, Wang J and Berndt C C 2013 Sol-gel synthesized copper-substituted cobalt ferrite nanoparticles for biomedical applications *J. Nano Res.* **22** 95–106
[46] Thakur P, Gahlawat N, Punia P, Kharbanda S, Ravelo B and Thakur A 2022 Cobalt nanoferrites: a review on synthesis, characterization, and applications *J. Supercond. Nov. Magn.* **35** 2639–69
[47] El-Masry M M, Mahmoud AE-r, Morshidy H Y and Ramadan R 2023 Cu^{2+}- and Zn^{2+}-doped cobalt spinel ferrite: insights on structural, thermal conduction, electric, magnetic and elastic properties *J. Mater. Sci., Mater. Electron.* **34** 383
[48] Thakur A, Verma R, Wan F, Ravelo B, Edelman I, Ovchinnikov S and Thakur P 2023 Investigation of structural, elastic and magnetic properties of Cu^{2+} ions substituted cobalt nano ferrites *J. Magn. Magn. Mater.* **581** 170980
[49] Mohamed W S, Hadia N M A, Al bakheet B, Alzaid M and Abu-Dief A M 2022 Impact of Cu^{2+} cations substitution on structural, morphological, optical and magnetic properties of $Co_{1-x}Cu_xFe_2O_4$ nanoparticles synthesized by a facile hydrothermal approach *Solid State Sci.* **125** 106841
[50] Hämmer M, Wessels V, Ettlinger R and Höppe H A 2021 Microwave-assisted hydrothermal synthesis, crystal structure, and thermal decomposition of strontium citrate monohydrate Sr3 (C6H5O7) 2 H2O *Z. Anorg. Allg. Chem.* **647** 204–9
[51] Kotsakis N, Raptopoulou C P, Tangoulis V, Terzis A, Giapintzakis J, Jakusch T and Salifoglou A 2003 Correlations of synthetic, spectroscopic, structural, and speciation studies in the biologically relevant cobalt (II)− citrate system: the tale of the first aqueous dinuclear cobalt (II)− citrate complex *Inorg. Chem.* **42** 22–31
[52] Matzapetakis M, Dakanali M, Raptopoulou C P, Tangoulis V, Terzis A, Moon N, Giapintzakis J and Salifoglou A 2000 Synthesis, spectroscopic, and structural characterization of the first aqueous cobalt(II)-citrate complex: toward a potentially bioavailable form of cobalt in biologically relevant fluids *J. Biol. Inorg. Chem.* **5** 469–74
[53] Yalçın B and Erbil C 2018 Effect of sodium hydroxide solution as polymerization solvent and activator on structural, mechanical and antibacterial properties of PNIPAAm and P(NIPAAm–clay) hydrogels *Polym. Compos.* **39** E386–406
[54] Imanipour P, Hasani S, Afshari M, Sheykh S, Seifoddini A and Jahanbani-Ardakani K 2020 The effect of divalent ions of zinc and strontium substitution on the structural and magnetic properties on the cobalt site in cobalt ferrite *J. Magn. Magn. Mater.* **510** 166941
[55] Auckett J E, Studer A J, Sharma N and Ling C D 2012 Floating-zone growth of brownmillerite Sr2Fe2O5 and the observation of a chain-ordered superstructure by single-crystal neutron diffraction *Solid State Ionics* **225** 432–6
[56] Abdel-Aal S K and Abdel-Rahman A S 2020 Graphene influence on the structure, magnetic, and optical properties of rare-earth perovskite *J. Nanopart. Res.* **22** 267
[57] Abdel-Aal S K, Beskrovnyi A I, Ionov A M, Mozhchil R N and Abdel-Rahman A S 2021 Structure investigation by neutron diffraction and x-ray diffraction of graphene nanocomposite CuO–rGO prepared by low-cost method *Physica Status Solidi (a)* **218** 2100138
[58] Abdel-Aal S K, Kandeel M F, El-Sherif A F and Abdel-Rahman A S 2021 Synthesis, characterization, and optical properties of new organic–inorganic hybrid perovskites [(NH3)2(CH2)3]CuCl4 and [(NH3)2(CH2)4]CuCl2Br2 *Physica Status Solidi (a)* **218** 2100036
[59] Için K, Öztürk S, Çakıl D D, Sünbül S E, Ergin İ and Özçelik B 2022 Investigation of nano-crystaline strontium hexaferrite magnet powder from mill scale waste by the mechanochemical synthesis: effect of the annealing temperature *Mater. Chem. Phys.* **290** 126513
[60] Icin K, Akyol S, Alptekin F, Yıldız A, Sünbül S E, Ergin İ and Öztürk S 2023 A comparative study of the correlation among the phase formation, crystal stability and magnetic properties of SrFe12-xMxO19 (M = Al3+, Cr3+ and Mn3+, x = 0–0.5) ferrite permanent magnets *J. Solid State Chem.* **324** 124126
[61] Abdel-Aal S K, Abdel-Rahman A S, Gamal W M, Abdel-Kader M, Ayoub H S, El-Sherif A F, Kandeel M, Bozhko S, Yakimov E and Yakimov E 2019 Crystal structure, vibrational spectroscopy and optical properties of a one-dimensional organic–inorganic hybrid perovskite of [NH3CH2CH (NH3) CH2] BiCl5 *J. Acta Crystallographica section B: Structural Science, Crystal Engineering* **75** 880–6
[62] Kandeel M F, Abdel-Aal S K, El-Sherif A F, Ayoub H S and Abdel-Rahman A S 2019 Crystal structure and optical properties of 1D-bi based organic-inorganic hybrid perovskite *IOP Conf. Ser.: Mater. Sci. Eng.* **610** 012063
[63] Sarmah S, Patra K P, Maji P K, Ravi S and Bora T 2023 A comparative study on the structural, magnetic and dielectric properties of magnesium substituted cobalt ferrites *Ceram. Int.* **49** 1444–63
[64] Belavi P B, Chavan G N, Naik L R, Somashekar R and Kotnala R K 2012 Structural, electrical and magnetic properties of cadmium substituted nickel–copper ferrites *Mater. Chem. Phys.* **132** 138–44
[65] Tabish T A, Ashiq M N, Ullah M A, Iqbal S, Latif M, Ali M, Ehsan M F and Iqbal F 2016 Biocompatibility of cobalt iron oxide magnetic nanoparticles in male rabbits *Korean J. Chem. Eng.* **33** 2222–7
[66] Gharibshahian M, Nourbakhsh M S and Mirzaee O 2018 Evaluation of the superparamagnetic and biological properties of microwave assisted synthesized Zn & Cd doped CoFe2O4 nanoparticles via Pechini sol–gel method *J. Sol-Gel Sci. Technol.* **85** 684–92
[67] Caizer C 2021 Theoretical study on specific loss power and heating temperature in CoFe2O4 nanoparticles as possible candidate for alternative cancer therapy by superparamagnetic hyperthemia *Applied Sciences* **11** 12
[68] Srinivasan S Y, Paknikar K M, Bodas D and Gajbhiye V 2018 Applications of cobalt ferrite nanoparticles in biomedical nanotechnology *Nanomedicine* **13** 1221–38
[69] Denzer M L, Mowery C, Comstock H A, Maheswarappa N B, Mafi G, VanOverebeke D L, Ramanathan R, Denzer M, Mowery C and Comstock H 2020 Characterization of the cofactors involved in non-enzymatic metmyoglobin/methemoglobin reduction *In Vitro J. Meat Muscle Biology* **4** 1
[70] Strader M B, Kassa T, Meng F, Wood F B, Hirsch R E, Friedman J M and Alayash A I 2016 Oxidative instability of hemoglobin E (β26 Glu→Lys) is increased in the presence of free α subunits and reversed by α-hemoglobin stabilizing protein (AHSP): relevance to HbE/β-thalassemia *Redox Biology* **8** 363–74

[71] Zhan J, Liu Q S, Zhang Y, Sun Z, Zhou Q and Jiang G 2023 Silica nanoparticles trigger phosphatidylserine exposure in red blood cells and induce thrombosis risk *Environ. Pollut.* **327** 121591
[72] Pradal J, Maudens P, Gabay C, Seemayer C A, Jordan O and Allémann E 2016 Effect of particle size on the biodistribution of nano-and microparticles following intra-articular injection in mice *Int. J. Pharm.* **498** 119–29
[73] Kim M J and Shin S 2014 Toxic effects of silver nanoparticles and nanowires on erythrocyte rheology *Food Chem. Toxicol.* **67** 80–6
[74] Liu T T *et al* 2009 A high speed detection platform based on surface-enhanced Raman scattering for monitoring antibiotic-induced chemical changes in bacteria cell wall *PLoS One* **4** e5470
[75] Yalcin B 2022 Exploration of the potential of Co/Cu co-doped Fe2O4 for medical applications: nanostructure, catalytic properties, and blood compatibility *J. Nanopart. Res.* **24** 271
[76] Ran Q, Xiang Y, Liu Y, Xiang L, Li F, Deng X and Li Z 2015 Eryptosis indices as a novel predictive parameter for biocompatibility of Fe3O4 magnetic nanoparticles on erythrocytes *Sci. Rep.* **5** 16209
[77] Tsui S M, Ahmed R, Amjad N, Ahmed I, Yang J, Manno F and Lau C 2020 Single red blood cell analysis reveals elevated hemoglobin in poikilocytes *J. Biomed. Opt.* **25** 015004–015004
[78] Hermosillo-Abundis C, Angulo-Molina A and Méndez-Rojas M A 2024 Erythrocyte vulnerability to airborne nanopollutants *Toxics* **12** 92
[79] Bashir S and Liu J 2015 Nanosafety: exposure, measurement, and toxicology *Advanced Nanomaterials and Their Applications in Renewable Energy* **367**
[80] Yang M, Zhou H, Cheng Y, Hong Q, Chen J, Zhang Q and Pan C 2022 Incorporation of copper and strontium ions in TiO2 nanotubes via dopamine to enhance hemocompatibility and cytocompatibility *Nanotechnology Reviews* **11** 1450–63
[81] Tsai S-W, Yu W-X, Hwang P-A, Huang S-S, Lin H-M, Hsu Y-W and Hsu F-Y 2018 Fabrication and characterization of strontium-substituted hydroxyapatite-CaO-CaCO3 nanofibers with a mesoporous structure as drug delivery carriers *Pharmaceutics* **10** 4
[82] Murugesan V, Vaiyapuri M and Murugeasan A 2022 Fabrication and characterization of strontium substituted chitosan modify hydroxyapatite for biomedical applications *Inorg. Chem. Commun.* **142** 109653
[83] Ayodele B V, Bin Mohd Yassin M Y, Naim R and Abdullah S 2019 Hydrogen production by thermo-catalytic conversion of methane over lanthanum strontium cobalt ferrite (LSCF) and αAl2O3 supported Ni catalysts *J. Energy Inst.* **92** 892–903
[84] Maurya J C, Janrao P S, Datar A A, Kanhe N S, Bhoraskar S V and Mathe V L 2016 Evidence of domain wall pinning in aluminum substituted cobalt ferrites *J. Magn. Magn. Mater.* **412** 164–71
[85] Mulyawan A, Dewi S H, Yunasfi W D S and Mashadi A W A 2023 The effects of lanthanum ions substitution on properties and effective absorption bandwidth (EAB) of zinc ferrite *J. Solid State Chem.* **327** 124275
[86] Liu M, Li J, Wang J, Yi H, Bao X and Gao X 2023 Effect of Mn and Zn binary Co-substitution on structure and magnetic properties of cobalt ferrites *Materials Science and Engineering:* **289** 116229
[87] kumar N H, Ravinder D and Edukondalu A 2022 Synthesis, structural, antimicrobial activity and dielectric properties of Ce3+-doped Ni–Zn nano-ferrites *Appl. Phys.* **128** 978